CELL BIOLOGY

Chaperone-mediated autophagy regulates adipocyte differentiation

Susmita Kaushik[1,2]*, Yves R. Juste[1,2], Kristen Lindenau[1,2], Shuxian Dong[1,2], Adrián Macho-González[1,2], Olaya Santiago-Fernández[1,2], Mericka McCabe[1,2,3], Rajat Singh[1,2,4], Evripidis Gavathiotis[2,3,4], Ana Maria Cuervo[1,2,4]*

Adipogenesis is a tightly orchestrated multistep process wherein preadipocytes differentiate into adipocytes. The most studied aspect of adipogenesis is its transcriptional regulation through timely expression and silencing of a vast number of genes. However, whether turnover of key regulatory proteins per se controls adipogenesis remains largely understudied. Chaperone-mediated autophagy (CMA) is a selective form of lysosomal protein degradation that, in response to diverse cues, remodels the proteome for regulatory purposes. We report here the activation of CMA during adipocyte differentiation and show that CMA regulates adipogenesis at different steps through timely degradation of key regulatory signaling proteins and transcription factors that dictate proliferation, energetic adaptation, and signaling changes required for adipogenesis.

INTRODUCTION

The adipose tissue is a major player in fat storage and metabolism. Adipocyte differentiation is a dynamic, tightly coordinated, and multifactorial process wherein preadipocytes transform into mature fat-storing adipocytes in response to lipid availability (*1*). The process of adipocyte differentiation consists of two phases: the commitment of multipotent mesenchymal stem cells to preadipocyte and the terminal differentiation of preadipocytes into adipocytes (*2*). Adipogenesis involves a temporally regulated pattern of gene expression events that drive the activation of pathways including cell proliferation, cellular energetics, and lipid synthesis. Sequential engagement of these processes is attained by the complex interplay between signaling molecules and transcription factors. Most of our understanding of adipocyte differentiation is through studies of gene expression profiles of the involved factors in cultured preadipocytes. However, whether coordinated and timed degradation of key regulatory proteins controls adipocyte differentiation remains undetermined.

Chaperone-mediated autophagy (CMA) is a selective protein degradation pathway in which proteins bearing a KFERQ-like motif are degraded in lysosomes upon recognition by the cytosolic chaperone heat shock cognate protein of 71 kDa (HSC70) (*3*). Upon arrival to lysosomes, substrates bind to the CMA receptor lysosome-associated membrane protein 2A (LAMP2A), which multimerizes to form a translocation complex for substrates to reach the lumen (*4*, *5*). CMA remodels the cellular proteome through the turnover of fully functional essential regulatory proteins to terminate their function. Previous studies identified as CMA substrates proteins involved in the regulation of glucose and lipid metabolism and cell cycle and in the initiation or termination of specific transcriptional programs (*3*). Given the diversity of proteins that can be selectively turned over by CMA, and the fact that some of these cellular pathways are timely activated or repressed during adipocyte differentiation, we hypothesized that CMA could participate in adipocyte differentiation through the timed degradation of regulatory proteins. CMA activity decreases gradually with age, and in response to sustained dietary lipid challenges, both conditions associated with defective adipogenesis, reduced preadipocyte capacity to differentiate, dysfunctional adipocyte-like cells, and adipose tissue dysfunction (*6*).

Here, we show that inactivation of basal CMA leads to blockage of adipocyte differentiation at the early commitment steps. Blockage of CMA in adipocyte precursors in mouse results in reduced fat mass with abnormally augmented cellular proliferation rates, increased inflammation, and fibrosis. We demonstrate that CMA drives adipogenesis by sequentially regulating cell cycle arrest, glycolysis, and specific transcriptional adipogenesis programs, through the coordinated degradation of limiting proteins in each of these processes. Our findings underscore the importance of functional CMA for adipogenesis.

RESULTS

CMA activity increases with adipocyte differentiation

To determine possible changes in CMA activity during adipogenesis, we used the preadipocyte line 3T3L1 that differentiates into adipocytes when treated with the adipogenic pharmacological agents, insulin, dexamethasone, and 3-isobutyl-1-methylxanthine (*7*). Adipocyte differentiation associated with increased LAMP2A mRNA and protein levels, but we did not observe an increase in other LAMP2 isoforms [Fig. 1, A and B; note that the apparent delay in the increase of LAMP2A protein levels relative to mRNA changes is an expected result of the complex maturation of the protein through the Golgi and its long half-life once in lysosomes (*8*)]. We found a time-dependent increase in CMA activity with adipocyte differentiation using a fluorescent CMA reporter (*9*) that, when delivered through CMA, highlights lysosomes as fluorescent puncta (Fig. 1C and fig. S1A). Costaining with the lysosomal marker LAMP1 confirmed KFERQ-Dendra$^+$ puncta as lysosomes and also revealed that the number of total lysosomes remained relatively constant through differentiation (fig. S1B). These findings support the combination of two different mechanisms, shown before to regulate CMA (*10*, *11*), to contribute to the observed increase in CMA during differentiation: (i) recruitment of lysosomes previously not engaged in CMA (LAMP1$^+$Dendra$^-$) to

[1]Department of Developmental and Molecular Biology, Albert Einstein College of Medicine, Bronx, NY, USA. [2]Institute for Aging Studies, Albert Einstein College of Medicine, Bronx, NY, USA. [3]Department of Biochemistry, Albert Einstein College of Medicine, Bronx, NY, USA. [4]Department of Medicine, Albert Einstein College of Medicine, Bronx, NY, USA.
*Corresponding author. Email: ana-maria.cuervo@einsteinmed.edu (A.M.C.); susmita.kaushik@einsteinmed.edu (S.K.)

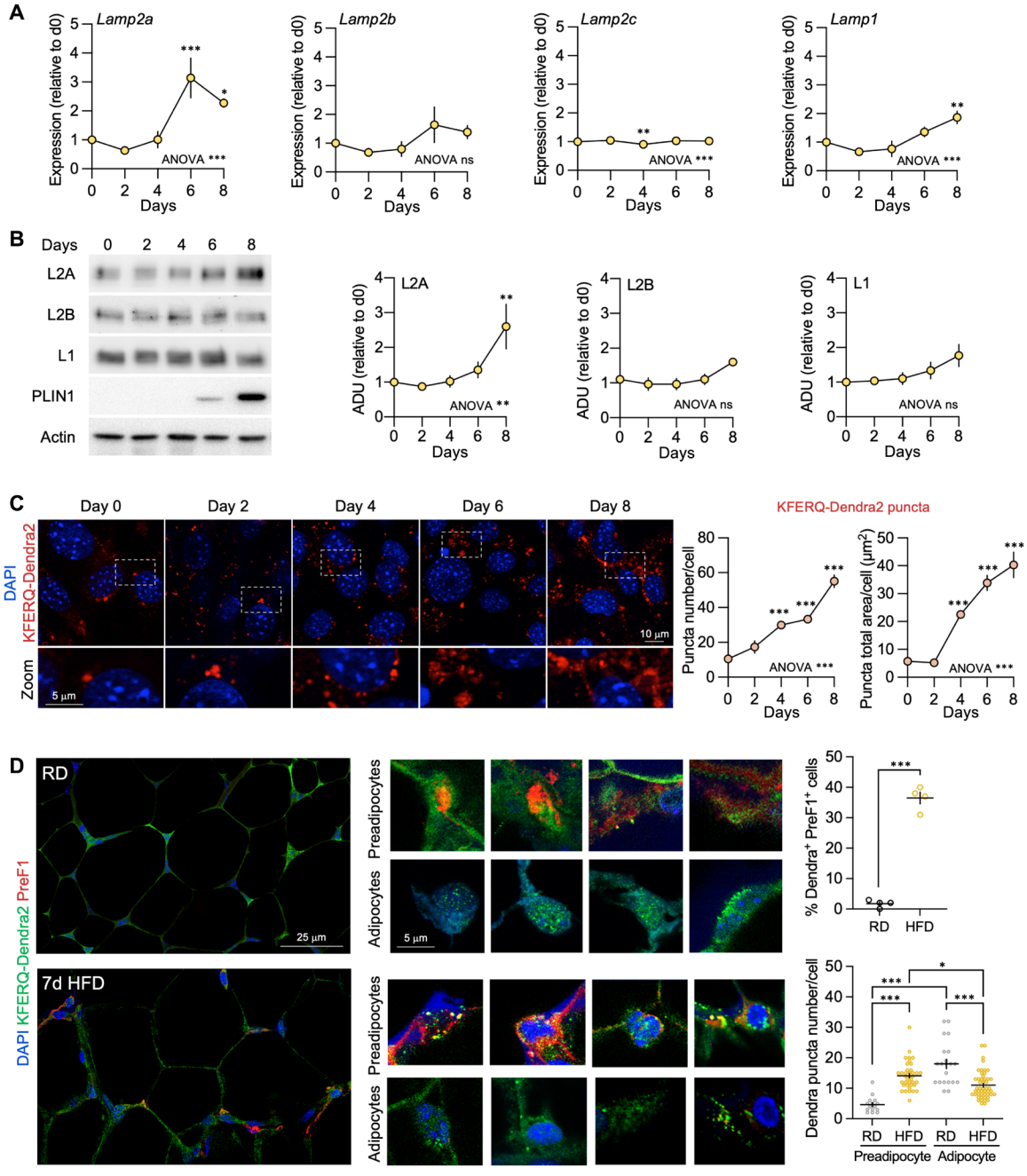

Fig. 1. CMA activity increases during adipocyte differentiation. (**A**) mRNA levels of indicated genes from 3T3L1 cells during adipocyte differentiation. $n = 6$ independent experiments (i.e.). (**B**) Representative immunoblots of indicated proteins from 3T3L1 cells during adipocyte differentiation (left) and quantification expressed as arbitrary densitometric units (ADU) relative to day 0 (right). $n = 4$ i.e. (**C**) Representative images of 3T3L1 cells stably expressing KFERQ-PS-Dendra2 reporter at the indicated times during adipocyte differentiation. Insets show boxed area at higher magnification. Nuclei are highlighted with 4′,6-diamidino-2-phenylindole (DAPI). Full-field images are shown in fig. S1A. Right: Quantification of CMA activity as number (left) or total area (right) of fluorescent puncta per cell. $n = 6$ i.e. with 40 cells each. (**D**) Immunostaining for PreF1 of eWAT from KFERQ-Dendra-mice maintained on regular diet (RD) or high-fat diet for 7 days (7d HFD). Left: Representative full-field images. Insets show higher-magnification images of preadipocytes and perinuclear region of adipocytes. Right: quantification of percentage of PreF1$^+$ cells displaying fluorescent puncta (top) and average number of fluorescent puncta per cell (bottom). Nuclei are highlighted with DAPI. $n = 4$ mice. Values are means ± SEM. $^*P < 0.05$, $^{**}P < 0.01$, $^{***}P < 0.001$, and ns $P > 0.05$ using one-way analysis of variance (ANOVA) (A to C), unpaired t test (D, top), and two-way ANOVA (D, bottom).

perform CMA (LAMP1$^+$Dendra$^+$), followed by (ii) transcriptional up-regulation and de novo synthesis of LAMP2A, the limiting CMA component. These sequential mechanisms for CMA up-regulation explain the observed activation of CMA (Fig. 1C) at times before the increase in LAMP2A protein (Fig. 1B) because LAMP2A is present in all type of lysosomes (active and inactive for CMA) and it is the lysosomal acquisition of the luminal HSC70 chaperone that makes them competent for CMA (*11*).

Similar activation of CMA also occurred in vivo during adipogenesis. We induced adipogenesis in a mouse model expressing the same CMA reporter (KFERQ-Dendra2 mice) (*12*) by feeding for 1 week a high-fat diet (HFD) (*13*). While as previously reported for other cells, HFD decreased CMA activity of differentiated adipocytes (preadipocyte factor 1; PreF1-negative), it induced CMA in adipocyte precursors (PreF1-positive) (Fig. 1D; only the perinuclear region of adipocytes is shown in the inserts to better appreciate the Dendra^{+} puncta). We conclude that preadipocytes display up-regulated CMA activity as they differentiate into adipocytes.

Blocking CMA impairs adipocyte differentiation

To determine whether preadipocyte CMA activity is required for their differentiation, we stably knocked down *lamp2a* in the preadipocyte cell line [L2A(−)] (Fig. 2A). By day 8 of induction of adipogenesis, 70% of control (CTR) cells had differentiated into adipocytes, but L2A(−) cells failed to differentiate as demonstrated by the absence of lipid droplets (LDs) in phase contrast, 1,6-diphenyl-1,3,5-hexatriene (DPH) staining, and undetectable perilipin 1 (PLIN1; specific adipocyte LD marker) (Fig. 2, B to G). Immunoblot and immunofluorescence revealed abnormally elevated levels of PLIN2 (small LD coat protein in preadipocytes) and no PLIN1 in the small LD observed in L2A(−) cells (Fig. 2, D and E).

To study the contribution of CMA to adipogenesis in vivo, we knocked out *lamp2a* specifically in the fibro/adipogenic progenitor cells that give rise to white adipocytes (*14*) by crossing LAMP2A$^{flox/flox}$ mice (*15*) with platelet-derived growth factor receptor–α (PDGFRα)–directed CRE mice (henceforth, LAMP2A knockout mice, ^{L2A}KO mice) that express CRE in most types of adipocyte progenitor cells (fig. S1C) (*14*, *16*). To study postnatal adipogenesis, we performed most of our studies in mice at 1 month of age. ^{L2A}KO mice had decreased epididymal white adipose tissue (eWAT) depot size and higher proportion of smaller cells compared to control (Fig. 2, H to J) but displayed no size or morphological changes in inguinal WAT (iWAT) (fig. S1, D and E). Control and ^{L2A}KO mice eWAT showed comparable oxygen consumption rates (OCR) (fig. S1F) excluding changes in energy expenditure as the cause of smaller eWAT cells in ^{L2A}KO mice. Chow-fed ^{L2A}KO mice eWAT showed a mild proinflammatory phenotype with increased macrophage content (Fig. 2K) and transcriptional up-regulation of proinflammatory genes, but not in the anti-inflammatory genes *IL10* and *Arginase 1* (fig. S1G). The ^{L2A}KO mice inflammatory phenotype was exacerbated when fed HFD, with increased eWAT levels of F4/80 and tumor necrosis factor–α (Fig. 2L) and of crown-like structures, a histological signature of macrophage infiltration in inflamed adipose tissue (Fig. 2M). Triglyceride accumulation in the liver from HFD-fed ^{L2A}KO mice (fig. S1H) suggests a possible failure of the inflamed adipose tissue to adequately store lipid. Because we show that there is no L2A loss in the liver of these ^{L2A}KO mice (fig. S1C), this hepatic lipid accumulation is likely due to the defect in adipose tissue, causing ectopic lipid deposition. Although one of the most widely used CRE drivers to study adipogenesis, PDGFRα expression is not exclusive to fibro/adipogenic progenitors and can also be detected in cells in the vasculature and in the central nervous system (*17*, *18*); however, the fact that we did not find any difference in vasculature in eWAT (fig. S1I) or in hypothalamus-regulated functions such as food intake (fig. S1J) in the ^{L2A}KO mice, at least at the age of our studies, suggests no contribution from these extra-adipose sites of potential L2A knockout. In further support of the lack of contribution of other cell types or organs to the observed adipose phenotype, we isolated primary preadipocytes from ^{L2A}KO mice. As we observed in the 3T3-L1 cell line, in vitro differentiation of primary preadipocytes from ^{L2A}KO mice eWAT depots also displayed reduced number of differentiated cells at day 9 (Fig. 2N and fig. S1K). These findings suggest that CMA controls adipogenesis in a cell-autonomous manner.

As in other cells and tissues (*15*, *19*–*22*), selective elimination of LAMP2A in preadipocytes both in vitro or in vivo did not interfere with macroautophagy (measured as light chain protein 3, LC3 II flux) (*23*) and did not result in compensatory up-regulation of this pathway, as in other cell types (fig. S1, L and M) (*15*, *19*). In summary, our findings show that blocking CMA in preadipocytes results in impaired adipocyte differentiation that associates with reduced fat mass and increased adipose inflammation.

CMA is important for preadipocyte commitment to differentiation

To identify the step(s) in the adipogenesis program dependent on CMA, we used the preadipocyte cell line because the adipogenic steps and timelines are well defined in this cell line (*1*). In support of defect at an early step of differentiation, L2A(−) cells showed down-regulation of the terminal adipocyte differentiation markers *PLIN1* and adipocyte protein 2 (*aP2*) and of the master adipogenesis drivers CCAAT/enhancer-binding protein alpha (*CEBP*α) and peroxisome proliferation-activated receptor γ (*PPAR*γ), while *CEBP*β expression by day 2 of differentiation was elevated and *CEBP*δ expression remained unchanged (Fig. 3A). The elevated levels of the preadipocyte genes delta-like noncanonical notch ligand 1 (*DLK1*) and GATA binding protein 3 (*GATA3*) in L2A(−) cells further support a defect in the initial step of adipogenesis (days 0 to 2) in these cells. Furthermore, using a small-molecule inhibitor of CMA (*24*) that we confirmed efficiently inhibits CMA in preadipocytes (fig. S2A), we found that blockage of CMA at different days after commitment (day 2, 4, or 6 onward) did not affect the differentiation of 3T3L1 cells, determined by BODIPY staining of LD and analysis of expression of *PLIN1* and *aP2* (fig. S2, B and C).

Similar to L2A(−) 3T3L1 cells, eWAT depots from the ^{L2A}KO mice also displayed aberrant abundance of preadipocytes—increased expression of preadipocyte markers *DLK1*, *KROX20*, *GATA2*, *GATA3*, and *TCF7L1* and lower expression of differentiated adipocyte genes *Leptin*, glucose transporter 4 (*GLUT4*), and *Adipoq* (Fig. 3, B and C). We attribute the absence of changes in adipocyte genes such as *PLIN1*, *CEBP*α, and *PPAR*γ in the ^{L2A}KO mice to the known heterogeneity of adipocyte progenitors in vivo. iWAT depots from the ^{L2A}KO mice at the same age show no significant differences in expression of adipocyte genes, although they display a significant increase in *KROX20* expression and trends to higher levels of other preadipocyte markers, albeit not significant and more modest than the ones observed in the eWAT of these animals (fig. S2D). Consistent with differentiation failure, ^{L2A}KO mice eWAT depots showed increased number of adipocyte precursors [Lin^{-}CD140^{+} cells (*25*) in stromal vascular fractions or PreF1^{+} cells in depot sections] (Fig. 3, D and E). Once again, we propose these changes in gene expression in the eWAT observed upon CMA blockage to be mostly of cell autonomous nature, because primary preadipocytes from ^{L2A}KO mice eWAT when differentiated in vitro displayed a significantly lower expression of most adipocyte genes analyzed, although, in this setting, only one preadipocyte gene (*GATA3*) was elevated in the ^{L2A}KO

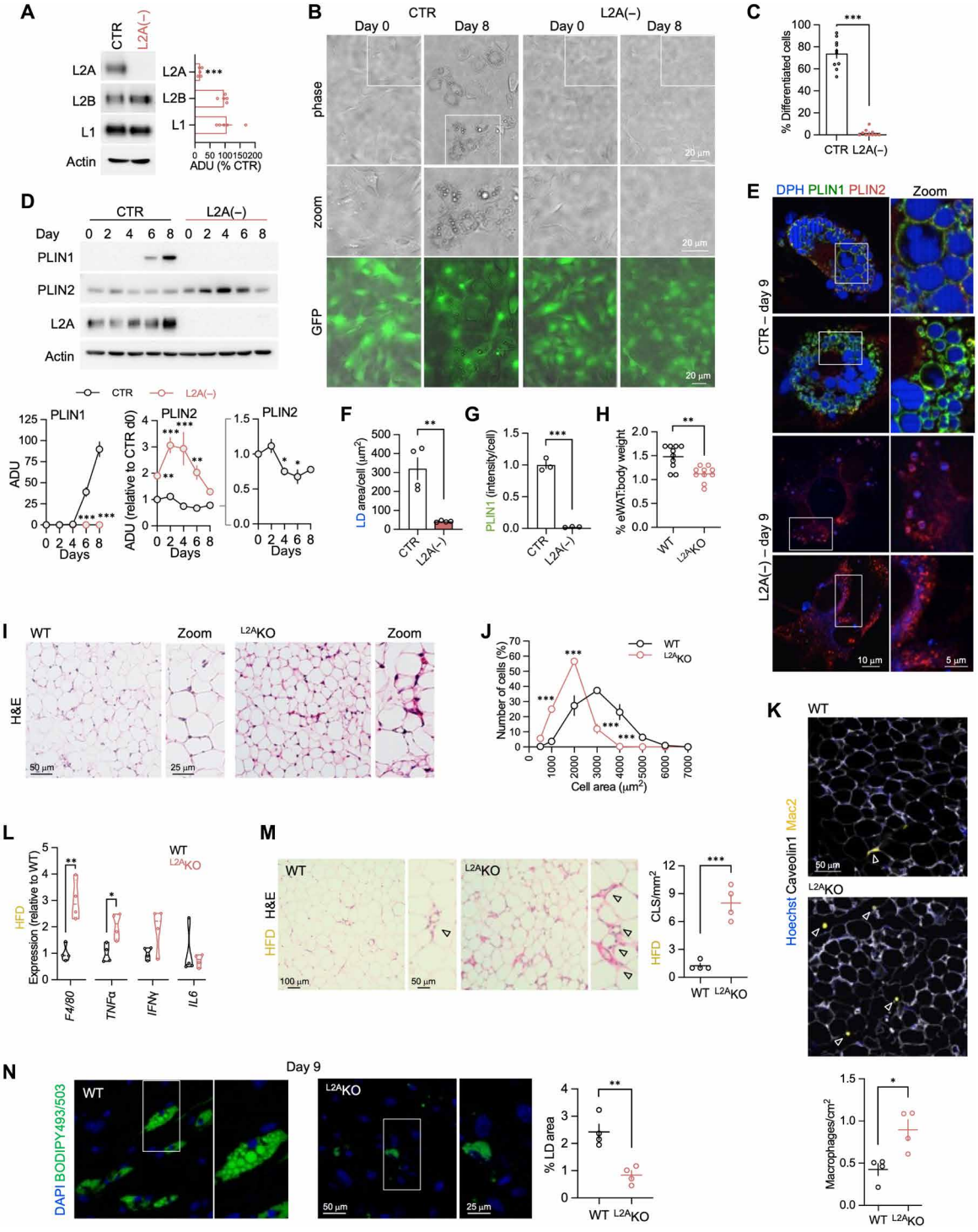

Fig. 2. Blocking CMA impairs adipocyte differentiation. (**A**) Immunoblot of 3T3L1 cells control (CTR) or stably knocked down for L2A [L2A(−)] and densitometric quantification. $n = 5$ i.e. (**B**) Phase contrast images at the indicated differentiation days. Green fluorescent protein (GFP) shows transduction efficiency. (**C**) Percentage of differentiated cells at day 8 from (B). $n = 10$ i.e. (**D**) Immunoblot of the indicated proteins and densitometric quantification during adipocyte differentiation. $n = 3 - 6$ i.e. (**E**) DPH, PLIN1, and PLIN2 staining at day 9 of adipocyte differentiation. (**F** and **G**) Quantification of area occupied by LD (F) and PLIN1 intensity (G) from (E). $n = 4$ (F) and 3 (G) i.e. (**H**) % eWAT/body weight for WT and L2AKO mice. $n = 10$ mice. (**I** and **J**) Hematoxylin and eosin (H&E) staining (I) and size distribution of cells (J) of eWAT. Zoom: Higher magnification. $n = 3$ mice. (**K**) eWAT immunostaining for Mac2 and caveolin1 and quantification of number of macrophages. Arrowheads: Macrophages ($Mac2^+$ cells). Nuclei are highlighted with Hoechst. $n = 4$ mice. (**L** and **M**) mRNA expression of indicated genes (L) and H&E staining (left) and quantification of crown-like structures (CLS; arrowheads) (right) (M) in eWAT from WT and L2AKO mice on HFD. $n = 4$ mice. (**N**) Staining for BODIPY 493/503 (to stain LD) and quantification of LD area in in vitro differentiated primary preadipocytes from WT and L2AKO mice eWAT at day 9. Nuclei are highlighted with DAPI. Full-field images are in fig. S1K. $n = 4$ mice with 15 fields each. All insets are boxed areas at higher magnification. Values are means ± SEM. $^*P < 0.05$, $^{**}P < 0.01$, and $^{***}P < 0.001$ using two-way ANOVA (D and J) or unpaired *t* test (the rest of the panels).

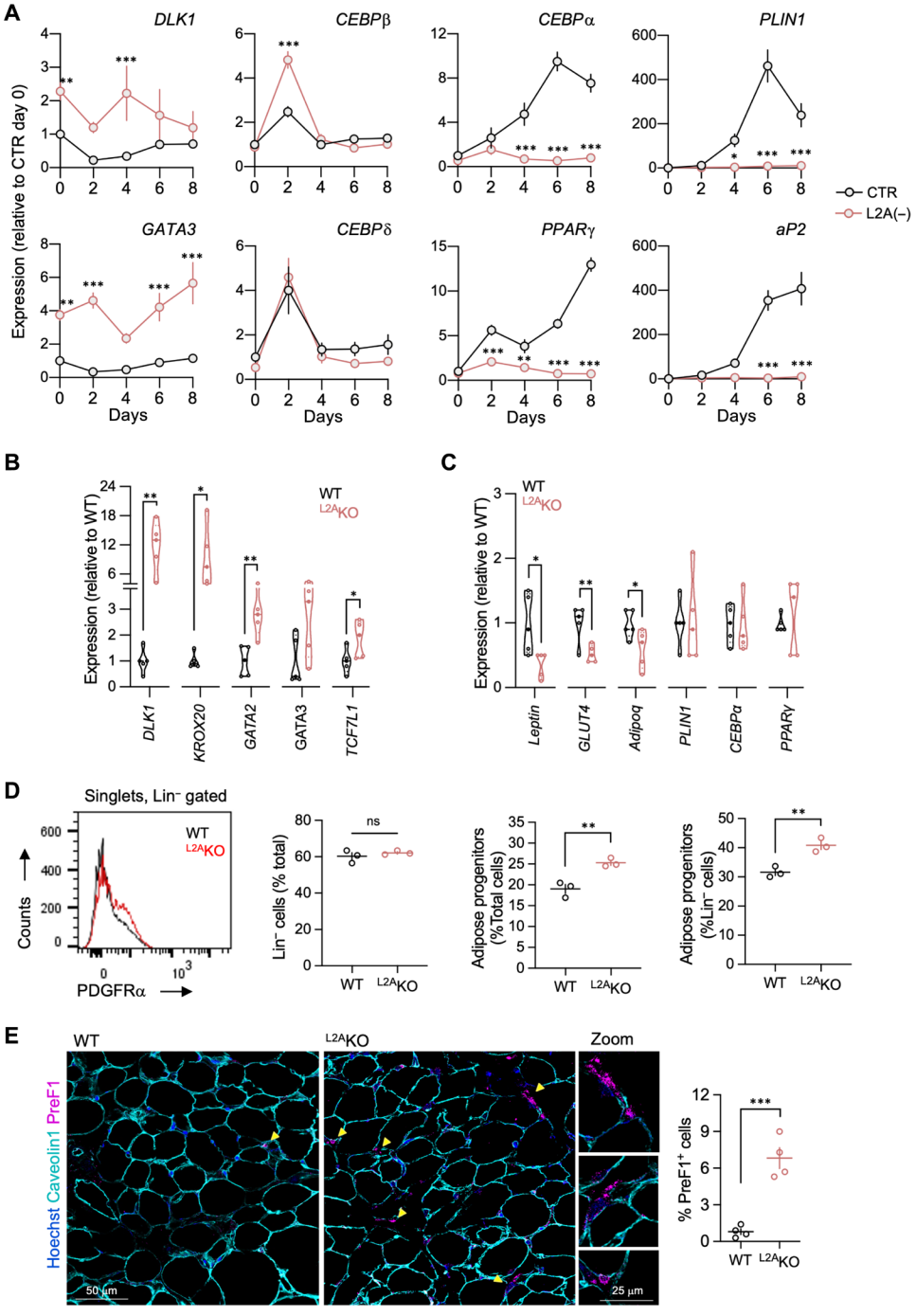

Fig. 3. CMA is required for preadipocyte commitment to differentiation. (**A**) mRNA expression of indicated genes of 3T3L1 cells control (CTR) or stably knocked down for *lamp2a* [L2A(–)] at indicated times of adipocyte differentiation. $n = 3$ to 10 i.e. (**B** and **C**) mRNA expression of indicated preadipocyte (B) and adipocyte (C) genes of eWAT from WT and L2AKO mice. $n = 5$ mice. (**D**) Flow cytometry for WT and L2AKO eWAT adipose progenitor cells showing percentage of Lin^- $PDGFR^+$ adipose progenitors. $n = 3$ mice. (**E**) Left: Immunostaining for PreF1 and caveolin1 of eWAT from WT and L2AKO mice. Arrowheads: $PreF1^+$ cells. Right: Quantification of percentage of $PreF1^+$ cells. Nuclei are highlighted with Hoechst. $n = 4$ mice. Values are means ± SEM. $^*P < 0.05$, $^{**}P < 0.01$, $^{***}P < 0.001$, and ns $P > 0.05$ using two-way ANOVA (A) and unpaired *t* test (B to E).

mice at day 9 of differentiation (fig. S2E). Consistent with these molecular and cellular aberrations, loss of CMA resulted in age-associated insulin-resistance (fig. S2F). Our studies show that CMA loss impairs the early stages of adipogenesis and results in accumulation of undifferentiated preadipocytes.

CMA regulated pathways in adipogenesis

To identify the protein substrates of CMA that accumulate in CMA-deficient preadipocytes, which could contribute to halted adipogenesis, we first focused on the persistence of PLIN2 in LD from L2A(–) preadipocytes (Fig. 2, D and E, and fig. S3A). As differentiation

progresses, large LD formation requires exchange of PLIN2/3 by PLIN1 (*26*). PLIN2 degradation by CMA has been described in nonadipose cells (*27*), whereby HSC70 detaches PLIN2 from the LD surface and promotes its transfer to lysosomes for degradation without exposure to the cytosol through kiss-and-run encounters between CMA active lysosomes and LD (*27*, *28*). The significant decrease in PLIN2 in control preadipocytes after day 2 of differentiation (Fig. 2D), coinciding with the increase in CMA activity, suggested that PLIN2 may undergo CMA degradation in preadipocytes. To test whether PLIN2 degradation by CMA was required for the PLIN2-to-PLIN1 exchange, we stimulated adipogenesis in control preadipocytes and, at day 3 (right before the time when *PLIN1* expression starts), transfected them with a plasmid expressing WT-PLIN2 or a previously described CMA-resistant mutant PLIN2 [missing the CMA targeting motif (*27*) and fig. S3B]. Cells expressing CMA-mutant PLIN2 failed to differentiate into adipocytes (fig. S3C), suggesting that the removal of PLIN2 from the growing LD occurs via CMA and it is required to progress to full differentiation. PLIN2 is also known to be degraded by the ubiquitin-proteasome system in differentiated adipocytes (*29*), and we also observed a discrete increase in levels of PLIN2 in our in vitro preadipocyte cultures upon addition of the proteasome inhibitor lactacystin, in support of some level of basal degradation of PLIN2 through the proteasome (fig. S3D). Proteasome degradation of PLIN2 was comparable between control and L2A(−) cells up to day 4 of differentiation when we found it to be decreased in L2A (−) cells (fig. S3D). This decrease in proteasome degradation seems specific for PLIN2 because the degradation rates of the pool of K48-specific ubiquitinated proteins were unchanged in CMA-deficient preadipocytes at all times tested (fig. S3E).

Because, besides PLIN2 persistence, we identified pronounced transcriptional changes in master adipogenesis drivers (Fig. 3), an event that precedes changes in LD morphology, we next tested whether CMA may also facilitate timely removal of key components earlier in the adipogenesis program. To identify proteins that may act as inhibitors of adipogenesis when not removed by CMA, we first analyzed cellular pathways disrupted in L2A(−) preadipocytes at days 0 and 2 of differentiation. Because the transcriptional profile of adipocyte differentiation in 3T3L1 cells has been well characterized and CMA has been shown to degrade specific transcription factors or their inhibitors (*3*) and to regulate transcriptional programs in other settings (*21*, *30*), we performed comparative transcriptomics. Transcriptional analysis revealed that L2A(−) cells had a blunted response to differentiation with only approximately 18 and 42% of the up-regulated and down-regulated genes coinciding with control cells (Fig. 4, A and B). We identified 143 genes that increased at basal levels and that failed to decrease in L2A(−) cells with differentiation, which were related to cell cycle, signaling pathways, and metabolism (Fig. 4, C to G). Many of the signaling pathways up-regulated in L2A(−) cells [such as Sirtuin, Wnt, and protein kinase A (PKA) signaling] are known to suppress preadipocyte differentiation (Fig. 4, D to G). The 52 genes that basally decreased in L2A(−) cells and that failed to increase at day 2 coded for proteins that participate in cytoskeleton, tight junction, and gap junction signaling among others (fig. S4, A to C).

To identify the specific CMA substrates important for adipogenesis regulation, we used the Ingenuity Pathway Analysis tool that predicts differentially activated upstream regulators from the transcriptional profile of L2A(−) and control cells. We identified 55 and 54 upstream activators (with z score $\geq$ 2), respectively (Fig. 4, H and J), with a majority of them (78 to 80%) bearing the CMA-targeting motif in their sequence (Fig. 4, I and K). Hierarchical mapping of these upstream regulators identified Myc and transforming growth factor–β (TGFβ) (Fig. 4, H and J, insets, and fig. S4, D and E) as the major proteins responsible for the transcriptional changes in downstream proliferation, metabolism, transcription, and signaling events required for adipogenesis.

Changes in the transcriptional profile of CMA-deficient preadipocytes matched in terms of overall z score, upstream regulators, and downstream effectors with profiles reported in human adipose tissue under experimental proinflammatory conditions or adipose from patients with common metabolic disorders such as obesity or diabetes (fig. S5A). Furthermore, comparison of the signature heatmap of CMA-deficient preadipocytes and the human disease adipose tissues also revealed matching in many entities (upstream regulators, downstream effectors, canonical pathways, and causal networks) (fig. S5B).

Overall, these findings support that CMA failure during adipogenesis prevents engagement and repression of specific transcriptional pathways previously proven essential for adipogenesis, namely, the proliferative burst, the metabolic switch, and the termination of TGFβ signaling.

CMA loss leads to sustained preadipocyte proliferation

Central to adipogenesis is the transition between cell proliferation and differentiation (*31*). Because our gene expression analyses predicted the upstream regulator of proliferation Myc, to be activated in L2A(−) cells (fig. S4D), we first evaluated the cell cycle state in control and L2A(−) cells during early stages of differentiation—when growth-arrested cells undergo one or two rounds of cell division for initiation and commitment to differentiation (*31*). Contrary to control cells that shift from 10 to 30% proliferating cells 24 hours after initiation of differentiation, 30% of L2A(−) preadipocytes were proliferating on day 0 and remained at 35% on day 1 (Fig. 5A). Similarly, eWAT depots from ^{L2A}KO mice also show elevated proliferation based on increased expression of *Cyclin D1* and increased Ki67 staining when compared to wild-type (WT) littermates (Fig. 5, B and C).

Because Myc bears two canonical CMA-targeting motifs (^{267}VEKRQ and ^{361}VLERQ) and its levels were elevated in L2A(−) cells at day 0 (Fig. 5D), we explored whether Myc could undergo CMA degradation during adipogenesis. Addition of lysosomal inhibitors in control cells revealed lysosomal degradation of Myc during adipogenesis that mirrored Myc transcriptional changes, whereby maximal transcriptional expression coincided with a decrease in Myc lysosomal degradation and down-regulation of transcription with a return to basal rates of lysosomal degradation (fig. S6B compared to fig. S6A). In contrast, lysosomal turnover of Myc was undetectable in L2A(−) cells, thus explaining its higher levels in these cells (fig. S6B). In agreement with previous studies (*32*), we noted that a substantial proportion of Myc is also degraded by the proteasome with a similar pattern to lysosomal degradation in control cells (fig. S6C). Despite proteasomal degradation of Myc remaining constant in L2A(−), we observed higher basal Myc nuclear levels in these cells, consistent with their proliferative phenotype (Fig. 5, E to G). Degradation of cytosolic Myc in lysosomes, observed in control cells, was not detected in L2A(−) cells, thus explaining their higher cytosolic levels (Fig. 5, E and F). We conclude that failure of CMA to degrade Myc, a key driver of cellular proliferation, is behind the increase in proliferation and dysregulation of cell cycle observed in CMA-defective preadipocytes.

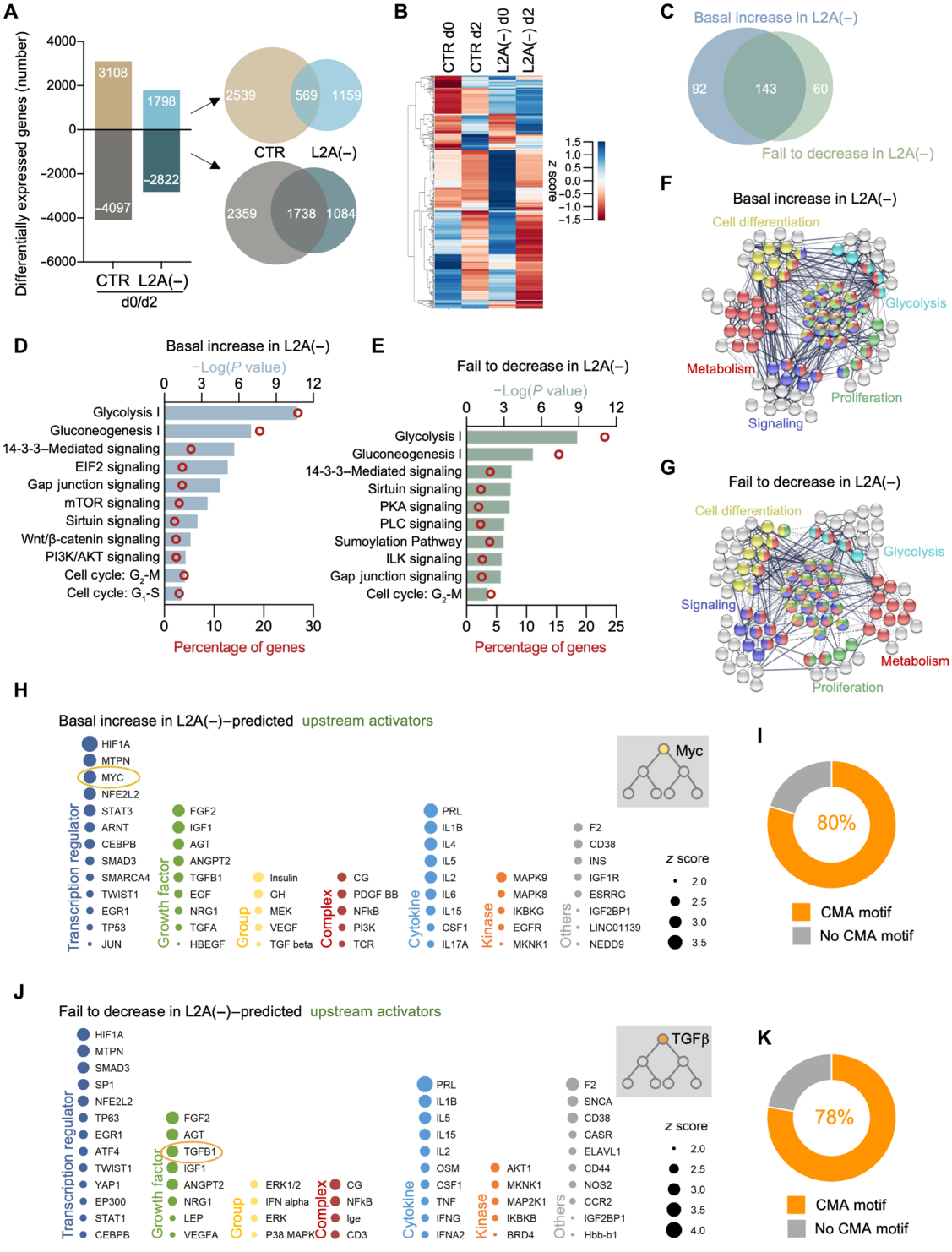

Fig. 4. CMA blockage deregulates functional pathways involved in adipocyte differentiation. (**A**) Differentially expressed genes in CTR and L2A(−) 3T3L1 cells, comparing days 0 and 2. Venn diagrams depict the up-regulated (top) and down-regulated (bottom) genes in the two cell lines. (**B**) Heatmap and hierarchical clustering analysis between CTR and L2A(−) cells at days 0 and 2 of differentiation. (**C**) Venn diagram of genes increased basally in L2A(−) cells and those that fail to decrease in L2A(−) with differentiation when compared to CTR. (**D** and **E**) Gene ontology enrichment analysis of genes with constitutively (basal) increased expression (D) or that fail to decrease with differentiation (E) in L2A(−) cells when compared to CTR. (**F** and **G**) Pathway enrichment analysis of genes with constitutively (basal) increased expression (F) or that fail to decrease expression with differentiation (G) in L2A(−) cells when compared to CTR. (**H** to **K**) Predicted upstream activators of genes with constitutively (basal) increased expression (H) or that fail to decrease expression with differentiation (J) in L2A(−) cells when compared to CTR. Hierarchical arrangement places Myc on top of upstream regulators constitutively activated in L2A(−) and TGFβ on top of upstream regulators that fail to decrease during differentiation [see detailed maps in fig. S4 (D and E)]. Percentage of proteins bearing CMA motifs (KFERQ-like motifs) among the proteins shown in (H) and (J) are shown in (I) and (K), respectively. All gene ontology terms are significant for $P < 0.001$.

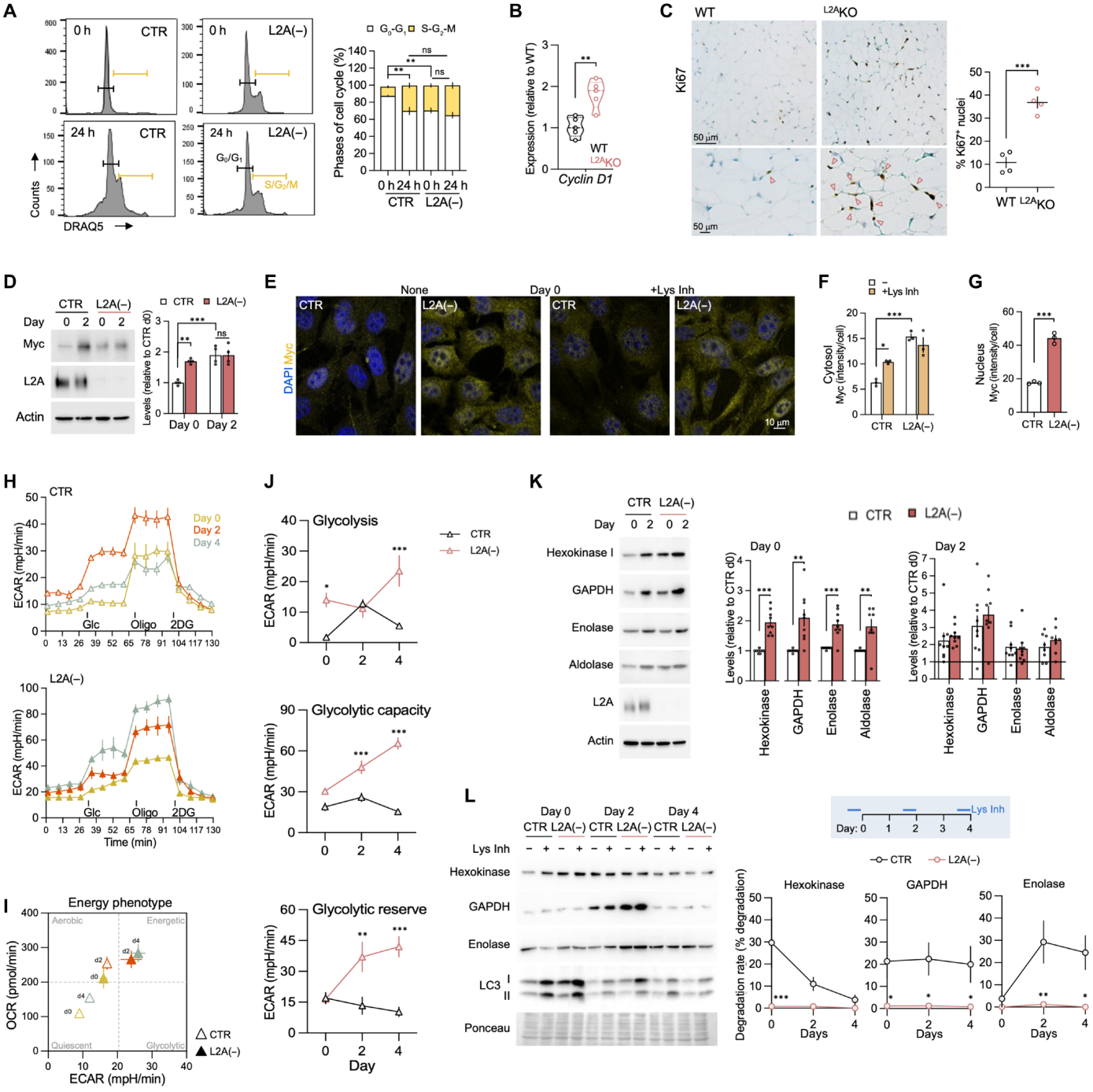

Fig. 5. Lack of CMA in preadipocytes leads to sustained proliferation and glycolysis during differentiation. (**A**) Cell cycle analysis of 3T3L1 cells control (CTR) or stably knocked down for *lamp2a* [L2A(–)] at days 0 and 1 of differentiation. Left: Representative histograms. Right: Quantification of phases of cell cycle. $n = 3$ i.e. (**B**) mRNA expression of indicated gene of eWAT. $n = 5$ mice. (**C**) Left: Immunostaining of eWAT for Ki67 and quantification of percentage of Ki67$^+$ cells (arrowheads). Insets: Higher magnification. $n = 4$ mice. (**D**) Immunoblot of CTR and L2A(–) 3T3L1 cells at indicated times of adipocyte differentiation (left) and quantification of protein levels (right). $n = 4$ i.e. (**E** to **G**) Immunostaining for Myc (E) and quantification of Myc levels in cytosol (F) and nuclei (G) in 3T3L1 cells at day 0 untreated or treated with inhibitors of lysosomal proteolysis (Lys Inh). Nuclei are highlighted with DAPI. $n = 3$ i.e. (**H** to **J**) Extracellular acidification rates (ECAR) (H), energy phenotype (I) and glycolysis, glycolytic capacity, and glycolytic reserve (J) in 3T3L1 cells CTR or L2A(–) at days 0 to 4 of differentiation. $n = 4$ i.e. (**K**) Immunoblot and quantification of 3T3L1 cells at indicated times of differentiation. $n = 9$ i.e. (**L**) Immunoblots and lysosomal degradation rates for indicated proteins in 3T3L1 cells untreated or treated with Lys Inh at indicated times of differentiation. LC3 is a positive control for Lys Inh. $n = 7$ i.e. Values are means ± SEM. $^*P < 0.05$, $^{**}P < 0.01$, $^{***}P < 0.001$, and ns $P > 0.05$ using two-way ANOVA (A, D, F, J, and L) and unpaired *t* test (B, C, G, and K).

Aberrant glycolysis contributes to defective differentiation of CMA-deficient preadipocytes

The clonal expansion of preadipocytes in the initial steps before differentiating into adipocytes requires a substantial energy burst (*33*). Glycolysis was the top transcriptionally up-regulated pathway in L2A(−) cells at the basal state that remained elevated upon differentiation (Fig. 4, D and E). We found that, while control cells showed an increase in glycolysis at day 2, which decreased by day 4 of differentiation to basal levels (Fig. 5, H to J), CMA-deficient cells displayed dysregulated glycolysis rates that did not respond to adipogenic cues of differentiation (Fig. 5, H to J). L2A(−) preadipocytes remained in the energetic phenotype quadrant throughout differentiation, instead of the transition from quiescent to energetic and back to the quiescent phenotype of control cells (Fig. 5I).

We propose that these rapid changes in glycolysis in control cells during adipogenesis may require a combination of transcriptional down-regulation and timely removal of the glycolytic enzymes to terminate their function, as reported in other tissues (*15*). Although most glycolytic enzymes in L2A(−) cells displayed higher basal protein levels (Fig. 5K), not all of them were transcriptionally up-regulated (fig. S7, A and B). Lysosomal degradation assays revealed that each of these glycolytic enzymes was degraded through CMA in control cells at a rate and timing unique for each enzyme (Fig. 5L; note that plotting represents the lysosomal degradation rate for each protein). By contrast, L2A(−) cells had negligible lysosomal degradation for these three glycolytic enzymes (Fig. 5L) that did not correlate with changes in their gene expression (fig. S7, A and B) and that explain why levels of these enzymes remained elevated by day 4, when they had returned to basal levels in control cells (fig. S7C). Studies with the proteasome inhibitor lactacystin revealed no significant differences between control and L2A(−) cells in the fraction of glycolytic enzymes degraded by the proteasome (fig. S7, D and E). While we found similar glycolysis activity in control and L2A(−) cells at day 2 of differentiation (Fig. 5J, top), in agreement with glycolytic enzymes reaching similar levels in both cell types (Fig. 5K), glycolytic capacity and reserve (Fig. 5J, middle and bottom) were markedly elevated in L2A(−) cells, suggesting that blockage of CMA may promote the higher activity of the glycolytic enzymes through mechanisms other than changes in their cellular levels [i.e., through changes in activator factors or in posttranslational modifications (*34*–*36*)].

In support of the timely nature of the CMA-imposed changes in glycolysis, which occurs only at a specific time during adipogenesis, the levels of these enzymes in adipose tissue of ^{L2A}KO mice were no longer elevated when compared to WT tissue (fig. S7F). The observed trend toward decreased levels of glycolytic enzymes in eWAT of ^{L2A}KO mice could be reactive to the reduced fat mass and more inflamed state of the tissue (Fig. 2, H to M), as also supported by the observed decreased expression of glycolytic and lipogenic enzymes (fig. S7G). Our findings indicate that CMA regulates glycolysis rates during adipogenesis and that failure to timely degrade glycolytic enzymes leads to uncontrolled glycolysis in preadipocytes and adipogenesis failure.

Timed inhibition of TGFβ/SMAD signaling by CMA is required for adipocyte differentiation

Hierarchical mapping of the comparative transcriptomics data from control and L2A(−) preadipocytes predicted TGFβ signaling to be the major upstream mediator of the downstream defects during the differentiation of CMA-deficient preadipocytes (Fig. 4J and fig. S4E). TGFβ inhibits adipogenesis in vitro (*37*) and associates with adipose tissue inflammation and fibrosis (*38*). We found that eWAT depots from ^{L2A}KO mice exhibited up-regulated expression for *TGF*β (Fig. 6A), and this activation of TGFβ associated with significantly increased eWAT fibrosis as determined by trichrome staining (Fig. 6B) and with increased expression of fibrosis-related genes and of *CD9*, known to associate with increased fibrogenesis (Fig. 6C) (*39*). Expectedly, the fibrogenic phenotype of ^{L2A}KO eWAT was exacerbated when mice were fed HFD (Fig. 6D).

eWAT depots of ^{L2A}KO mice and L2A(−) preadipocytes at day 2 of differentiation displayed elevated levels of phosphorylated SMAD homolog 2/3 (SMAD2/3), downstream effectors of TGFβ that inhibit the positive feedback loop between the master regulators of adipogenesis PPARγ and CEBPα (Fig. 6, E and F) (*40*, *41*). Because SMAD2/3 have a phosphorylation-dependent CMA-targeting motif (^{409}KVLTQ), we assessed their lysosomal degradation and found substantial degradation of this protein by lysosomes at days 0 and 2 in control cells detected both by immunoblot and immunofluorescence and as higher colocalization with lysosomal markers, which were largely abolished in L2A(−) cells (Fig. 6, G to I, and fig. S8A). Changes in proteasomal degradation cannot account for the increase in SMAD2/3 levels in L2A(−) cells (fig. S8B). As anticipated, persistently higher cytosolic levels of SMAD2/3 in L2A(−) cells resulted in significantly elevated nuclear content of SMAD2/3 in these cells (Fig. 6J and fig. S8C).

To determine whether sustained elevated TGFβ/SMAD signaling was responsible for the differentiation failure of L2A(−) preadipocytes, we pharmacologically attenuated this signaling with the TGFβ inhibitor SB525334 administered for 12 hours before the adipocyte commitment phase and found that this intervention was enough to partially rescue the adipogenic defect of L2A(−) cells (Fig. 6K and fig. S8D). These findings suggest that CMA plays a key role in adipocyte differentiation by temporally suppressing TGFβ SMAD signaling in preadipocytes. To analyze the possible interdependence of the observed changes in TGFβ signaling and glycolysis in preadipocytes upon CMA blockage, we first up-regulated glycolysis in control cells with ML265, a glycolysis activator. We found that glycolysis up-regulation, to mimic the one observed in L2A(−) cells, did not result in significant changes in TGFβ signaling (fig. S8, E and F). Next, we inhibited TGFβ signaling in control cells and found a mild increase in glycolysis (fig. S8G) in support of the idea that the elevated TGFβ signaling observed in L2A(−) cells was not directly responsible for the observed up-regulated glycolysis in these cells. In summary, our studies have identified CMA as a major orchestrator of three distinct time-dependent nodes—proliferation, metabolism, and transcriptional regulation—each of which contributes to essential aspects of adipocyte differentiation.

DISCUSSION

We have identified a key role for CMA in adipocyte differentiation that relies on the selective and timely degradation to terminate the function of proteins involved in cellular proliferation (Myc), energetics (glycolytic enzymes), and transcriptional regulation (SMAD2/3) (fig. S9). Although maximal CMA activity is reached by day 6 of adipogenesis, functional CMA is necessary from the earlier stages during the determination phase of adipogenesis. Our data support that termination of specific cellular pathways required for adipogenesis progression is achieved not only by the transcriptional down-regulation

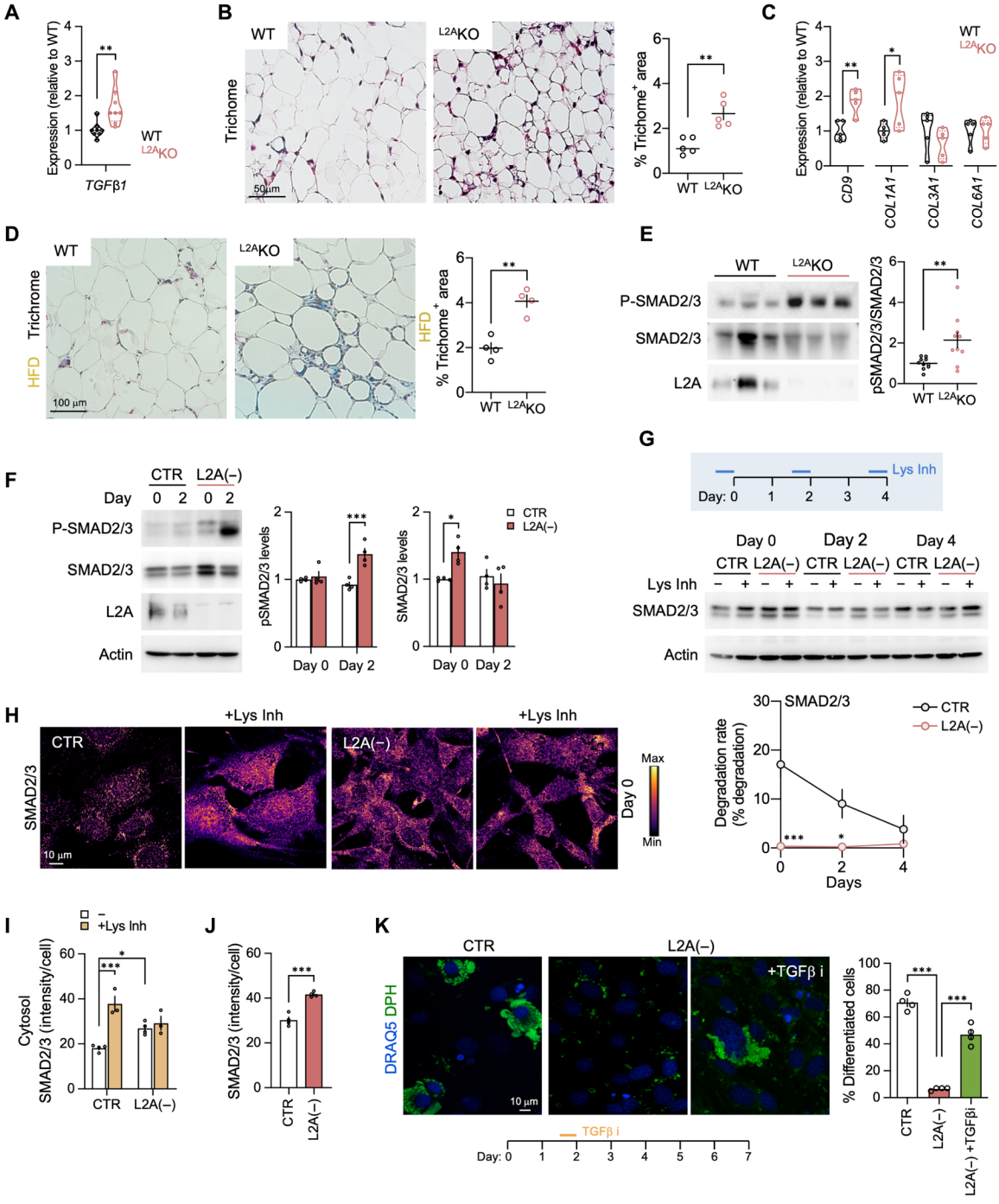

Fig. 6. Dysregulated TGFβ signaling is responsible for the adipogenesis defect in CMA-deficient preadipocytes. (**A**) mRNA expression of indicated gene of eWAT from WT and L2AKO mice. $n = 8$ mice. (**B**) Trichrome A staining of eWAT and quantification of percentage of Trichrome$^+$ area. $n = 5$ mice. (**C**) mRNA expression of indicated genes in eWAT. $n = 5$ mice. (**D**) Trichrome A staining of eWAT from WT and L2AKO mice on HFD and quantification of percentage of Trichrome$^+$ area. $n = 4$ mice. (**E**) Representative immunoblots for indicated proteins from eWAT of WT and L2AKO mice and quantification. $n = 10$ mice. (**F**) Representative immunoblots for indicated proteins and quantification of CTR and L2A(–) 3T3L1 cells at indicated times of adipocyte differentiation. $n = 4$ i.e. (**G**) Representative immunoblots and quantification of SMAD2/3 lysosomal degradation rates in CTR and L2A(–) 3T3L1 cells untreated or treated with Lys Inh at indicated times of adipocyte differentiation. $n = 7$ i.e. (**H** to **J**) Immunostaining of SMAD2/3 (H) and quantification of SMAD2/3 levels in cytosol (I) and nuclei (J) in 3T3L1 cells at day 0 untreated or treated with Lys Inh. Image shows color mapping by gradient intensity. $n = 3 - 4$ i.e. (**K**) DPH staining and quantification of percentage of differentiated cells in 3T3L1 cells at day 7 untreated or treated with TGFβ inhibitor for 12 hours at day 1.5. $n = 4$ i.e. Values are means ± SEM. $^*P < 0.05$, $^{**}P < 0.01$, and $^{***}P < 0.001$ using unpaired *t* test (A to E and J), two-way ANOVA (F, G, and I), and one-way ANOVA (K).

of genes in that pathway but also through the selective degradation of key regulatory proteins coded by those genes. In this study, we demonstrate that CMA regulates the duration of diverse cellular processes critical for adipogenesis completion.

A role for macroautophagy in adipocyte differentiation has been reported (*42*–*44*), but CMA and macroautophagy are nonredundant, and each of them contributes to specific aspects of adipogenesis. Macroautophagy-defective mice display reduced WAT mass, increased fat browning, mitochondrial enrichment, elevated fatty acid oxidation, and no changes in adipocyte progenitor numbers (*42*, *43*). Inhibition of macroautophagy after development results instead in eWAT inflammation, mitochondrial dysfunction, and insulin resistance without affecting adiposity (*44*). Studies on mouse models with macroautophagy inhibition specifically in PDGFRα$^+$ progenitor cells (using PDGFRα-CreERT2) have reported protection against HFD-induced adipose fibrogenesis and increase in adipose browning (*45*). In contrast, the phenotype of CMA deficiency in PDGFRα$^+$ progenitors is dominated by reduced fat mass, disruption of early phase of adipogenesis with increased number of adipose progenitors, elevated proliferation, increased inflammation and fibrogenesis, and no changes in browning or fatty acid oxidation. Similarly, the ubiquitin proteasome system also contributes to adipogenesis (*46*) through degradation of CEBPα and PPARγ (*47*–*51*). In the case of CMA-deficient preadipocytes, we observed rerouting of some of the identified CMA substrates to the proteasome (i.e., Myc and SMAD2/3) but not for others (i.e., enolase, GAPDH and hexokinase). However, even for the CMA substrates rerouted to the proteasome because proteasome degradation occurred at different times than by CMA, the functional defect in adipogenesis was not prevented. These findings highlight the unique roles of distinct autophagy pathways and the proteasome in adipogenesis, with each pathway catering to a specific cellular function. In this work, we noted that CMA blockage in iWAT led to a more discrete phenotype than the one observed in eWAT. Future studies are needed to discriminate whether these differences are a consequence of other cell lineages compensating early on in iWAT development or due to adipose depot-specific roles of CMA.

Despite the gradual increase in CMA activity as preadipocyte differentiation progresses, the fact that blockage of CMA even before it becomes up-regulated blunts the adipogenesis process highlights that basal CMA activity is necessary and sufficient for the initiation of adipogenesis. Later stages in the adipogenic program may require up-regulation of preadipocyte CMA above the normal basal levels to accommodate the larger number of proteins targeted for degradation, as remodeling of the proteome of a preadipocyte to become an adipocyte becomes more extensive. In this work, we have identified that adipogenesis-related changes in three different processes—signaling, proliferation, and glycolysis—require fully functional CMA. A multifunctional effect of this nature is expected for a proteolytic pathway when considering the functional variety of substrate proteins, and it highlights the role of protein degradation in the regulation of cellular functioning.

Reduced adipogenesis, like the one we observed in both in vitro and in vivo models of CMA-deficiency, associates with up-regulation of the preadipocyte marker, PreF1, which per se is known to inhibit adipogenesis (*52*). In addition, many of the known inhibitors of adipocyte differentiation (such as TGFβ, SMAD3, Wnt, Sirtuin, PKA, and GATA2/3) (*53*) were also up-regulated in our CMA-deficient models. We propose that termination of TGFβ/SMAD3 signaling may be one of the main mechanisms behind the regulatory effect of CMA on adipocyte differentiation, because pharmacological inhibition of TGFβ was effective in rescuing adipocyte differentiation in the CMA-defective models.

The remarkable coincidences between the transcriptional profile of CMA-defective preadipocytes and human adipose tissue from common metabolic conditions closely related to the metabolic syndrome of aging, and the fact that CMA blockage in preadipocytes results in impaired adipogenesis, increased adipocyte progenitors, hyperplasia, inflammation, and fibrosis in the adipose tissue, make attractive the possibility that age-related decline of CMA activity in preadipocytes may contribute to the adipose tissue dysfunction characteristic of old organisms.

MATERIALS AND METHODS

Mice

Adipose progenitor-specific LAMP2A KO mice (L2AKO) were generated by crossing C57BL/6 PDGFRα-Cre mice (JAX mice, stock 013148) with C57BL/6 L2A$^{f/f}$ mice (*15*). The control experimental group (named WT) was composed of either L2A$^{f/f}$ or PDGFRα-Cre littermate mice as no differences were detected among them. Most experiments were done with 4- to 5-week-old mice (when eWAT development is completed, and to rule out any compensatory changes that may occur with age in L2AKO mice). HFD experiments were done with 14-week-old mice that were on HFD (60% kcal from fat; Research Diets, D12492) for 8 weeks. KFERQ-Dendra2 transgenic mice (*12*) at 4 weeks of age were given HFD for 7 days. Only males were used in this study owing to the important differences in female metabolism that will require a full study on its own. All mice were genotyped at weaning, and genotyping was reconfirmed postmortem to correct for any possible misplacement during husbandry. Mice were all in the C57BL/6J background and housed in ventilated cages with no more than five mice per cage on a 12-hour light/12-hour dark cycle at 23°C with free access to water and food in the institutional barrier facility along with sentinel cages and were specific pathogen–free. All mouse procedures were approved by the Institutional Animal Care and Use Committee of Albert Einstein College of Medicine.

Cells

3T3-L1 murine preadipocyte cells (American Type Culture Collection, CL173) stably transduced with lentiviral vectors for control, knockdown of *lamp2a* (*54*), or KFERQ-Dendra2 CMA reporter (*9*, *12*) were maintained in Dulbecco's modified Eagle's medium (DMEM) (Sigma-Aldrich, D5648) supplemented with 10% fetal bovine serum (FBS) (Thermo Fisher Scientific, 35010CV) and antibiotics (Thermo Fisher Scientific, 15240112) at 37°C and 5% CO_2. The 3T3-L1 cell line was authenticated by karyotyping at regular intervals to confirm their identity and tested for mycoplasma contamination using a DNA staining protocol with Hoechst 33258 dye (Invitrogen, H3570) (weekly) or the MycoSenser PCR Assay Kit (monthly). All cells used in the present study were free of such contamination.

Reagents

Sources of chemicals and antibodies including dilutions are indicated in table S1. We have also provided catalog numbers or clone numbers for all the commercial antibodies in table S1. Most antibodies used are commercial and have been chosen on the basis of extensive use in the literature. When available, antibodies were validated

using cell lines knocked down for the antibody target (i.e., in the case of antibodies against LAMP2A, we used cell lines and tissues knocked down or tissues from knockout mice as negative controls).

Cell treatments

Adipocyte differentiation was initiated by culturing confluent cells in adipogenic induction medium consisting of the growth medium supplemented with 160 nM insulin (Sigma-Aldrich, I9278), 250 nM dexamethasone (Sigma-Aldrich, D4902), and 0.5 mM 1-methyl-3-isobutylxanthine (IBMX, Sigma-Aldrich, I7018) (day 0). Forty-eight hours later (day 2), the cells were switched to maintenance medium supplemented just with insulin. After 48 hours (day 4), the cells were placed back in unsupplemented maintenance medium, which was changed every 48 hours. For lysosomal flux assays, cells were treated with 20 mM ammonium chloride (Sigma-Aldrich, AX12701) or 100 μM leupeptin (Thermo Fisher Scientific, BP266225) for 12 hours at the indicated time points in differentiation. For proteasomal flux assays, cells were treated with lactacystin (5 μM; Enzo Life Sciences, BMLPI104) for 12 hours at the indicated time points, and efficacy of inhibition was monitored by tracking changes in K48-ubiquitinated proteins. TGFβ inhibitor (SB525334, Tocris, 3211) was added to differentiating cells at day 1.5 at 1 μM for 12 hours. ML265 (Cayman Chemical, 13942) was added to activate glycolysis in control cells at 1 and 2 μM for 12 hours.

Cell imaging

Cells grown on coverslips were fixed with 4% paraformaldehyde for 30 min, permeabilized, and blocked with 1% bovine serum albumin (BSA) and 0.01% Triton X-100 in phosphate-buffered saline (PBS). Incubation with primary and secondary antibodies conjugated to fluorophore in 0.1% BSA in PBS was performed at room temperature for 1 hour each. For LD staining, cells were incubated with DPH (5 μM; Sigma-Aldrich, D208000) or BODIPY 493/503 (20 μg/ml; Thermo Fisher Scientific, D3922) for 20 min at 37°C before fixation. For cells expressing CMA reporter (KFERQ-Dendra2), cells grown on coverslips were photoconverted (green to red) with a 405/20-nm LED array (Norlux) for 3 min using a light intensity of 50 mW/cm^2. Cells were fixed 16 hours later and processed for immunofluorescence as described above. Where indicated, coverslips were mounted in 4′,6-diamidino-2-phenylindole–Fluoromount-G (Southern Biotechnology, 0100-20) or incubated with DRAQ5 (Cell Signaling Technology, 4084) to stain the nucleus. For phase microscopy, live cells growing in six-well plates were used. Images were acquired with an Axiovert 200 fluorescence microscope (Carl Zeiss Microscopy) mounted with an ApoTome.2 slider or a Leica TCS SP8 confocal microscope using 40× or 63× objective and 1.4 numerical aperture. Images were prepared, and channels were given pseudo-colors (in some instances) and quantified using ImageJ (National Institutes of Health). The number and area of puncta were quantified using "analyze particles" or "3D object counter" (ImageJ) after thresholding in nonsaturated images. The percentage of colocalization was determined by "JACoP" plugin (ImageJ) after thresholding of individual channels (*55*). Fire lookup table (LUT) was used for color mapping by gradient intensity. Fluorescence intensity in nucleus/cytoplasm was measured by highlighting the nucleus/cell boundary using "free hand" tool (ImageJ). Antibodies used for cell imaging were LAMP2 (1:500; Developmental Studies Hybridoma Bank, GL2A7), Myc (1:800; Cell Signaling Technology, 5605), PLIN1 (1:400; Cell Signaling Technology, 9349), PLIN2 (1:400; PROGEN Biotechnik, GP40), and SMAD2/3 (1:500; Cell Signaling Technology, 8685).

Tissue imaging

The Histology and Comparative Pathology Core at Albert Einstein College of Medicine performed the tissue embedding and processing according to standard protocols. Paraffin-embedded sections (5 μm thick) of formalin-fixed adipose tissues were subjected to hematoxylin and eosin (H&E) staining and trichrome staining as per standard protocols. Sections were imaged using Leica light microscope DMD108. Morphometric analysis of cell size was performed on H&E sections using the "cell magic wand" tool in ImageJ. Cell area of 250 to 300 cells per section was determined. Immunostainings of eWAT sections were performed by citric acid–based antigen retrieval at 95°C for 30 min (Vector Laboratories, H-3300) of paraffin-embedded tissues, followed by permeabilization and blocking in PBS with 5% goat serum, 3% BSA, and 0.3% Triton X-100 for 1 hour at room temperature, and by incubation with primary antibody and fluorophore-conjugated secondary antibody prepared in 3% BSA and 0.1% Triton X-100 overnight at 4°C and 1 hour at room temperature, respectively. After antibody incubation, the tissue sections were washed five times in PBS and counterstained with Hoechst 33342 (1:2000) for 1 hour at room temperature. For whole-mount tissue imaging, approximately 2-mm^3 sections of eWAT depots dissected from CMA reporter mice were fixed with buffered zinc formalin (ANATECH, 171) at room temperature overnight followed by permeabilization, blocking, and antibody stainings as mentioned above. Images were acquired with a Leica TCS SP8 confocal microscope as mentioned above. Antibodies used for tissue imaging were caveolin1 (1:1000; Cell Signaling Technology, 3267), CD31 (1:200; Cell Signaling Technology, 77699), Ki67 (1:500; Abcam, ab15580), Mac2 (1:400; Thermo Fisher Scientific, 13-5301-82), and PreF1 (1:500; Sigma-Aldrich, MABN671).

Reverse transcription polymerase chain reaction

Total RNA was isolated with RLT buffer (QIAGEN) for cells and with TRIzol (Invitrogen, 79306) for tissues (whole eWAT fat pad) and by using the RNeasy Plus mini kit (QIAGEN, 74134) according to the manufacturer's instructions. Genomic DNA was excluded using a gDNA eliminator spin column. Total RNA (1 μg) was reverse-transcribed into cDNA using Superscript III (Invitrogen, 18080051), and quantitative reverse transcription polymerase chain reaction (RT-PCR) analyses were performed using Power SYBR Green PCR master mix (Applied Biosystems) on a StepOne Plus real-time PCR System (Applied Biosystems). Normalization of expression was performed with TATA-binding protein (*TBP*) as housekeeping gene. The mRNA expression in control samples was represented as 1, and mRNA expression in experimental samples was represented as fold change compared to expression in controls. The primers used are presented in table S2.

Immunoblot

Cell or tissue (whole eWAT fat pad) lysates were prepared in radioimmunoprecipitation assay buffer [150 mM sodium chloride, 1% NP-40, 0.5% sodium deoxycholate, 0.1% sodium dodecyl sulfate, and 50 mM tris (pH 8)] containing protease and phosphatase inhibitors. Protein concentration was measured by the Lowry method using BSA as a standard, and samples were subjected to SDS–polyacrylamide gel electrophoresis and immunoblotted after transfer to nitrocellulose membranes using standard procedures. Proteins were visualized by

using peroxidase-conjugated secondary antibodies and chemiluminescent reagent (PerkinElmer) in a G-BOX Chemi XX6 (Imgen). Unsaturated images were used for densitometry with ImageJ. The percentage of lysosomal degradation for specific proteins was calculated by discounting from the total amount of protein (given an arbitrary value of 100) the percentage of increase in protein levels upon addition of lysosomal inhibitors. Antibodies used for immunoblotting were actin (1:10,000; Abcam, AC15), aldolase (1:1000; Cell Signaling Technology, 3188), enolase 1 (1:1000; Cell Signaling Technology, 3810), glyceraldehyde-3-phosphate dehydrogenase (1:1000; Cell Signaling Technology, 2118), hexokinase (1:1000; Cell Signaling Technology, 2024), LAMP1 (1:3000; Developmental Studies Hybridoma Bank, 1D4B), LAMP2A (1:5000; Invitrogen, 512200, AMC2), LAMP2B (1:2000; generated in our laboratory), LC3 (1:1000; Cell Signaling Technology, 2775), Myc (1:1000; Cell Signaling Technology, 5605), PLIN2 (1:2000; PROGEN Biotechnik, GP40), SMAD2/3 (1:1000; Cell Signaling Technology, 8685), phospho-SMAD2/3 (1:1000; Cell Signaling Technology, 8828), and K48-specific ubiquitin (1:2000; Millipore Sigma, 051307, Apu2).

Glycolysis stress test

Extracellular acidification rates were measured using a 24-well Seahorse Bioanalyzer according to the manufacturer's instructions (Agilent Technologies). Cells were grown on gelatin-coated XF24 plate and subjected to differentiation in a staggering manner—so that CTR and L2A(−) cells at different days of differentiation were on the same plate. For glycolysis stress test, cells were shifted to base medium supplemented with 2 mM L-glutamine and incubated in a CO_2-free chamber at 37°C for 1 hour. Once in the bioanalyzer, plates were sequentially injected with 25 mM glucose, 2 μM oligomycin, and 100 mM 2-deoxyglucose. Glycolysis, glycolysis capacity, glycolytic reserve, and energy phenotype were calculated using Wave software as per the manufacturer's instructions.

Tissue respirometry

OCR of eWAT were measured using Seahorse Bioanalyzer XF24 (Agilent Technologies). Briefly, freshly excised tissue explants (8 to 12 mg) were placed in an islet-capture plate in Krebs-Henseleit buffer (111 mM sodium chloride, 4.7 mM potassium chloride, 2 mM magnesium sulfate, 1.2 mM disodium hydrogen phosphate, 0.5 mM carnitine, 2.5 mM glucose, and 10 mM sodium pyruvate). Basal OCR was measured followed by injection of permeabilization agent (digitonin, 0.05 μg/ml). Values were normalized to tissue weight.

Flow cytometry

For cell cycle analysis, centrifuged cells were resuspended in 1 μM DRAQ5 in PBS and incubated for 10 min at room temperature before analysis using a flow cytometer (BD LSR II analyzer). Histograms were deconvoluted by FlowJo software into G_0-G_1, S, and G_2-M peaks. Flow cytometric analysis for adipocyte precursors was performed as described previously (*25*). Excised whole eWAT fat pad was digested in collagenase type 2 (0.8 mg/ml; Worthington Biochemical, LS4174) in Hanks' balanced salt solution (HBSS) containing 3% BSA, 1.2 mM calcium chloride, 1.0 mM magnesium chloride, and 0.8 mM zinc chloride for 12 hours in a 37°C shaking water bath. Centrifugation at 300*g* for 3 min yielded the stromal vascular fraction pellet that was resuspended in 3% BSA in HBSS buffer and sequentially filtered through 70-μm (BD Biosciences, 352350) and 40-μm (BD Biosciences, 352340) filters before staining with the following antibodies for 20 min on ice: CD45-allophycocyanin eFluor 780 (1:5000; Thermo Fisher Scientific, 47-0451-80), CD31 phycoerythrin (1:500; Thermo Fisher Scientific, 12-0311-81), and CD140a/PDGFRα fluorescein isothiocyanate (1:400; Thermo Fisher Scientific, 11-1401-80). Following antibody incubation, samples were washed, centrifuged at 300*g* for 3 min, and analyzed with a BD LSR II analyzer. Data analysis was performed using FlowJo software. Lin^- cells were defined as $CD31^-$ $CD45^-$. Adipose progenitor cells are defined as Lin^- $PDGFR\alpha^+$ cells. The gating strategy is shown in fig. S3F.

Microarray and analysis

Total RNA was extracted from cells at days 0 and 2 using an RNeasy mini kit (QIAGEN) according to the manufacturer's protocols and submitted to Phalanx Biotech for analysis. Quality check was performed by Agilent RNA 6000 Nano Assay, and the array was performed using Agilent Mouse Micro Array 8x60k. Array raw data files were processed with the Rosetta Resolver System. Gene clustering by average linkage algorithm was performed on selected expression gene lists and normalized by *z* score after data transformation and mean centering. Gene set enrichment analyses were run using the weighted enrichment. The gene sets were analyzed for gene ontology, pathway enrichment, upstream regulators, and analysis match using the Ingenuity Pathway Analysis software (QIAGEN) and STRING database (https://string-db.org/). KFERQ-like motifs in predicted upstream regulator proteins were identified using the KFERQ Finder v0.8 database (https://rshine.einsteinmed.edu) (*56*).

Macroautophagy flux assay

Cells were untreated or treated with lysosomal protease inhibitors, ammonium chloride (20 mM), and leupeptin (100 μM) for 12 hours. For ex vivo flux, freshly excised tissue explants were incubated with high-glucose DMEM in the presence or absence of lysosomal protease inhibitors, ammonium chloride (20 mM), and leupeptin (200 μM) at 37°C and 5% CO_2 for 2 hours. Afterward, cells or tissue explants were homogenized in a lysis buffer containing protease inhibitors and processed for immunoblot for LC3. Macroautophagy flux was calculated by dividing the densitometry value of LC3 II in lysosomal-inhibitor treated by that of untreated samples.

Isolation and differentiation of primary preadipocytes

Primary preadipocytes were isolated from eWAT depots from WT and L2AKO mice using a preadipocyte isolation kit (Abcam, ab196988) according to the manufacturer's instructions. The preadipocytes were cultured in DMEM/F12, supplemented with 10% FBS and 1% penicillin/streptomycin, at 10% CO_2. To induce adipogenesis, confluent cultures were treated with adipogenesis induction cocktail [growth medium supplemented with insulin (1.5 μg/ml), 1 μM dexamethasone, 500 μM IBMX, and 1 μM rosiglitazone] for 3 days. After 3 days, the cells were maintained in growth medium with insulin (1.5 μg/ml). Cells were used at day 9.

Other methods

For transfection with PLIN2-tGFP WT or CMA-mutant (mutated KFERQ-motif) (*27*), 3T3L1 cells were transfected with 1 μg of plasmid DNA using Lipofectamine 2000 (Invitrogen, 11668027). Liver triglyceride content was assessed using a commercial kit (BioVision, K622) according to the manufacturer's instructions. Daily food

intake was measured in individually housed mice for five consecutive days. Residual food after 24 hours was subtracted from the added food to reveal daily food intake. Blood glucose in overnight fasted mice was measured using a glucometer (Bayer). Serum insulin in overnight fasted mice was measured using enzyme-linked immunosorbent assay (Crystal Chemicals, 90080). HOMA-IR was calculated using the standard calculations: HOMA-IR = Insulin (μIU/ml) × glucose (mmol/l)/22.5.

Quantification, statistics, and software

As indicated in the figure legends, all quantitative data are presented as the means ± SEM of biologically independent experiments or samples (referred to as *n* in the figure legends). All measurements were taken from distinct samples. For data from mice, individual values are also shown. Power analysis was used to determine the number of animals required for each analysis based on the previous biochemical and histological differences that we have found when manipulating CMA in the in vitro system or in other in vivo studies. With the calculated sample size and a two-sided type 1 error rate of 5%, >80% power was predicted to detect effects >1.5 in the parameters analyzed. None of the animals were excluded from the study. Animals inside the group control and the group LAMP2A KO were randomly assigned to control or HFD using the randomization function in Excel. Every experiment was performed in at least three independent replicates. Experiments in cells in culture were performed on different days to confirm reproducibility of the procedures. In addition, markers of adipocyte differentiation were used for each of the differentiation experiments and percentage of cells differentiated in the control cells were monitored to assure success of the differentiation protocol. Data collection and analyses were done blinded to the samples. Blinding was lifted only for the final statistical analysis. The following software were used: ImageJ for imaging and immunoblot analysis, Ingenuity Pathway Analysis (QIAGEN) and STRING database (https://string-db.org/) for cellular pathway enrichment, prediction of upstream regulators and analysis match, and FlowJo for flow cytometry analysis. Graphical plots were made using GraphPad Prism 9.0, R, and FlowJo v10.6.1, and the images were assembled using ImageJ v1.53f. Statistical analyses were performed using GraphPad Prism 9.0. Before statistical testing, normality was assessed using the Shapiro-Wilk test. Outliers were determined by the ROUT method ($Q = 1\%$). Statistical significance was compared by two-tailed unpaired Student's *t* test for two groups, one-way analysis of variance (ANOVA) followed by Dunnett's multiple comparisons test, or two-way ANOVA followed by Šídák's or Tukey's multiple comparisons test for multiple groups with $^{*}P < 0.05$, $^{**}P < 0.01$, $^{***}P < 0.001$, and ns (nonsignificant) representing $P > 0.05$.

SUPPLEMENTARY MATERIALS

Supplementary material for this article is available at https://science.org/doi/10.1126/sciadv.abq2733

View/request a protocol for this paper from *Bio-protocol*.

REFERENCES AND NOTES

1. Q. Q. Tang, M. D. Lane, Adipogenesis: From stem cell to adipocyte. *Annu. Rev. Biochem.* **81**, 715–736 (2012).
2. E. D. Rosen, O. A. MacDougald, Adipocyte differentiation from the inside out. *Nat. Rev. Mol. Cell Biol.* **7**, 885–896 (2006).
3. S. Kaushik, A. M. Cuervo, The coming of age of chaperone-mediated autophagy. *Nat. Rev. Mol. Cell Biol.* **19**, 365–381 (2018).
4. A. M. Cuervo, J. F. Dice, A receptor for the selective uptake and degradation of proteins by lysosomes. *Science* **273**, 501–503 (1996).
5. U. Bandyopadhyay, S. Kaushik, L. Varticovski, A. M. Cuervo, The chaperone-mediated autophagy receptor organizes in dynamic protein complexes at the lysosomal membrane. *Mol. Cell. Biol.* **28**, 5747–5763 (2008).
6. J. L. Kirkland, T. Tchkonia, T. Pirtskhalava, J. Han, I. Karagiannides, Adipogenesis and aging: Does aging make fat go MAD? *Exp. Gerontol.* **37**, 757–767 (2002).
7. H. Green, M. Meuth, An established pre-adipose cell line and its differentiation in culture. *Cell* **3**, 127–133 (1974).
8. A. M. Cuervo, J. F. Dice, Unique properties of lamp2a compared to other lamp2 isoforms. *J. Cell Sci.* **113**, 4441–4450 (2000).
9. H. Koga, M. Martinez-Vicente, F. Macian, V. V. Verkhusha, A. M. Cuervo, A photoconvertible fluorescent reporter to track chaperone-mediated autophagy. *Nat. Commun.* **2**, 386 (2011).
10. R. Kiffin, C. Christian, E. Knecht, A. M. Cuervo, Activation of chaperone-mediated autophagy during oxidative stress. *Mol. Biol. Cell* **15**, 4829–4840 (2004).
11. A. M. Cuervo, J. F. Dice, E. Knecht, A population of rat liver lysosomes responsible for the selective uptake and degradation of cytosolic proteins. *J. Biol. Chem.* **272**, 5606–5615 (1997).
12. S. Dong, C. Aguirre-Hernandez, A. Scrivo, C. Eliscovich, E. Arias, J. J. Bravo-Cordero, A. M. Cuervo, Monitoring spatiotemporal changes in chaperone-mediated autophagy in vivo. *Nat. Commun.* **11**, 645 (2020).
13. E. Jeffery, C. D. Church, B. Holtrup, L. Colman, M. S. Rodeheffer, Rapid depot-specific activation of adipocyte precursor cells at the onset of obesity. *Nat. Cell Biol.* **17**, 376–385 (2015).
14. R. Berry, M. S. Rodeheffer, Characterization of the adipocyte cellular lineage in vivo. *Nat. Cell Biol.* **15**, 302–308 (2013).
15. J. L. Schneider, Y. Suh, A. M. Cuervo, Deficient chaperone-mediated autophagy in liver leads to metabolic dysregulation. *Cell Metab.* **20**, 417–432 (2014).
16. Z. Gao, A. C. Daquinag, F. Su, B. Snyder, M. G. Kolonin, PDGFRα / PDGFRβ signaling balance modulates progenitor cell differentiation into white and beige adipocytes. *Development* **145**, dev155861 (2018).
17. S. Morikawa, Y. Mabuchi, Y. Kubota, Y. Nagai, K. Niibe, E. Hiratsu, S. Suzuki, C. Miyauchi-Hara, N. Nagoshi, T. Sunabori, S. Shimmura, A. Miyawaki, T. Nakagawa, T. Suda, H. Okano, Y. Matsuzaki, Prospective identification, isolation, and systemic transplantation of multipotent mesenchymal stem cells in murine bone marrow. *J. Exp. Med.* **206**, 2483–2496 (2009).
18. L. E. Rivers, K. M. Young, M. Rizzi, F. Jamen, K. Psachoulia, A. Wade, N. Kessaris, W. D. Richardson, PDGFRA/NG2 glia generate myelinating oligodendrocytes and piriform projection neurons in adult mice. *Nat. Neurosci.* **11**, 1392–1401 (2008).
19. A. C. Massey, S. Kaushik, G. Sovak, R. Kiffin, A. M. Cuervo, Consequences of the selective blockage of chaperone-mediated autophagy. *Proc. Natl. Acad. Sci. U.S.A.* **103**, 5805–5810 (2006).
20. R. Valdor, E. Mocholi, Y. Botbol, I. Guerrero-Ros, D. Chandra, H. Koga, C. Gravekamp, A. M. Cuervo, F. Macian, Chaperone-mediated autophagy regulates T cell responses through targeted degradation of negative regulators of T cell activation. *Nat. Immunol.* **15**, 1046–1054 (2014).
21. S. Dong, Q. Wang, Y. R. Kao, A. Diaz, I. Tasset, S. Kaushik, V. Thiruthuvanathan, A. Zintiridou, E. Nieves, M. Dzieciatkowska, J. A. Reisz, E. Gavathiotis, A. D'Alessandro, B. Will, A. M. Cuervo, Chaperone-mediated autophagy sustains haematopoietic stem-cell function. *Nature* **591**, 117–123 (2021).
22. M. Bourdenx, A. Martín-Segura, A. Scrivo, J. A. Rodriguez-Navarro, S. Kaushik, I. Tasset, A. Diaz, N. J. Storm, Q. Xin, Y. R. Juste, E. Stevenson, E. Luengo, C. C. Clement, S. J. Choi, N. J. Krogan, E. V. Mosharov, L. Santambrogio, F. Grueninger, L. Collin, D. L. Swaney, D. Sulzer, E. Gavathiotis, A. M. Cuervo, Chaperone-mediated autophagy prevents collapse of the neuronal metastable proteome. *Cell* **184**, 2696–2714.e25 (2021).
23. D. J. Klionsky *et al.*, Guidelines for the use and interpretation of assays for monitoring autophagy (3rd edition). *Autophagy* **12**, 1–222 (2016).
24. R. Gomez-Sintes, Q. Xin, J. I. Jimenez-Loygorri, M. McCabe, A. Diaz, T. P. Garner, X. M. Cotto-Rios, Y. Wu, S. Dong, C. A. Reynolds, B. Patel, P. de la Villa, F. Macian, P. Boya, E. Gavathiotis, A. M. Cuervo, Targeting retinoic acid receptor alpha-corepressor interaction activates chaperone-mediated autophagy and protects against retinal degeneration. *Nat. Commun.* **13**, 4220 (2022).
25. C. D. Church, R. Berry, M. S. Rodeheffer, Isolation and study of adipocyte precursors. *Methods Enzymol.* **537**, 31–46 (2014).
26. N. E. Wolins, D. L. Brasaemle, P. E. Bickel, A proposed model of fat packaging by exchangeable lipid droplet proteins. *FEBS Lett.* **580**, 5484–5491 (2006).
27. S. Kaushik, A. M. Cuervo, Degradation of lipid droplet-associated proteins by chaperone-mediated autophagy facilitates lipolysis. *Nat. Cell Biol.* **17**, 759–770 (2015).
28. S. Kaushik, A. M. Cuervo, AMPK-dependent phosphorylation of lipid droplet protein PLIN2 triggers its degradation by CMA. *Autophagy* **12**, 432–438 (2016).

29. Y. Takahashi, A. Shinoda, H. Kamada, M. Shimizu, J. Inoue, R. Sato, Perilipin2 plays a positive role in adipocytes during lipolysis by escaping proteasomal degradation. *Sci. Rep.* **6**, 20975 (2016).
30. J. Madrigal-Matute, J. de Bruijn, K. van Kuijk, D. F. Riascos-Bernal, A. Diaz, I. Tasset, A. Martín-Segura, M. J. J. Gijbels, B. Sander, S. Kaushik, E. A. L. Biessen, S. Tiano, M. Bourdenx, G. J. Krause, I. M. Cracken, A. H. Baker, H. Jin, N. E. S. Sibinga, J. J. Bravo-Cordero, F. Macian, R. Singh, P. C. N. Rensen, J. F. P. Berbée, G. Pasterkamp, J. C. Sluimer, A. M. Cuervo, Protective role of chaperone-mediated autophagy against atherosclerosis. *Proc. Natl. Acad. Sci. U.S.A.* **119**, e2121133119 (2022).
31. Q. Q. Tang, T. C. Otto, M. D. Lane, Mitotic clonal expansion: A synchronous process required for adipogenesis. *Proc. Natl. Acad. Sci. U.S.A.* **100**, 44–49 (2003).
32. M. A. Gregory, S. R. Hann, c-Myc proteolysis by the ubiquitin-proteasome pathway: Stabilization of c-Myc in Burkitt's lymphoma cells. *Mol. Cell Biol.* **20**, 2423–2435 (2000).
33. O. A. MacDougald, M. D. Lane, Transcriptional regulation of gene expression during adipocyte differentiation. *Annu. Rev. Biochem.* **64**, 345–373 (1995).
34. J.-Y. Zhang, F. Zhang, C.-Q. Hong, A. E. Giuliano, X.-J. Cui, G.-J. Zhou, G.-J. Zhang, Y.-K. Cui, Critical protein GAPDH and its regulatory mechanisms in cancer cells. *Cancer Biol. Med.* **12**, 10–22 (2015).
35. S. R. Maran, K. Fleck, N. M. Monteiro-Teles, T. Isebe, P. Walrad, V. Jeffers, I. Cestari, E. J. R. Vasconcelos, N. Moretti, Protein acetylation in the critical biological processes in protozoan parasites. *Trends Parasitol.* **37**, 815–830 (2021).
36. I. Mor, E. C. Cheung, K. H. Vousden, Control of glycolysis through regulation of PFK1: Old friends and recent additions. *Cold Spring Harb. Symp. Quant. Biol.* **76**, 211–216 (2011).
37. R. A. Ignotz, J. Massagué, Type beta transforming growth factor controls the adipogenic differentiation of 3T3 fibroblasts. *Proc. Natl. Acad. Sci. U.S.A.* **82**, 8530–8534 (1985).
38. T. Khan, E. S. Muise, P. Iyengar, Z. V. Wang, M. Chandalia, N. Abate, B. B. Zhang, P. Bonaldo, S. Chua, P. E. Scherer, Metabolic dysregulation and adipose tissue fibrosis: Role of collagen VI. *Mol. Cell. Biol.* **29**, 1575–1591 (2009).
39. G. Marcelin, A. Ferreira, Y. Liu, M. Atlan, J. Aron-Wisnewsky, V. Pelloux, Y. Botbol, M. Ambrosini, M. Fradet, C. Rouault, C. Henegar, J. S. Hulot, C. Poitou, A. Torcivia, R. Nail-Barthelemy, J. C. Bichet, E. L. Gautier, K. Clement, A PDGFRα-mediated switch toward CD9 ^{high} adipocyte progenitors controls obesity-induced adipose tissue fibrosis. *Cell Metab.* **25**, 673–685 (2017).
40. L. Choy, R. Derynck, Transforming growth factor-β inhibits adipocyte differentiation by Smad3 interacting with CCAAT/enhancer-binding protein (C/EBP) and repressing C/EBP transactivation function. *J. Biol. Chem.* **278**, 9609–9619 (2003).
41. Y. Tsurutani, M. Fujimoto, M. Takemoto, H. Irisuna, M. Koshizaka, S. Onishi, T. Ishikawa, M. Mezawa, P. He, S. Honjo, Y. Maezawa, Y. Saito, K. Yokote, The roles of transforming growth factor-β and Smad3 signaling in adipocyte differentiation and obesity. *Biochem. Biophys. Res. Commun.* **407**, 68–73 (2011).
42. R. Singh, Y. Xiang, Y. Wang, K. Baikati, A. M. Cuervo, Y. K. Luu, Y. Tang, J. E. Pessin, G. J. Schwartz, M. J. Czaja, Autophagy regulates adipose mass and differentiation in mice. *J. Clin. Invest.* **119**, 3329–3339 (2009).
43. Y. Zhang, S. Goldman, R. Baerga, Y. Zhao, M. Komatsu, S. Jin, Adipose-specific deletion of autophagy-related gene 7 (atg7) in mice reveals a role in adipogenesis. *Proc. Natl. Acad. Sci. U.S.A.* **106**, 19860–19865 (2009).
44. J. Cai, K. M. Pires, M. Ferhat, B. Chaurasia, M. A. Buffolo, R. Smalling, A. Sargsyan, D. L. Atkinson, S. A. Summers, T. E. Graham, S. Boudina, Autophagy ablation in adipocytes induces insulin resistance and reveals roles for lipid peroxide and Nrf2 signaling in adipose-liver crosstalk. *Cell Rep.* **25**, 1708–1717.e5 (2018).
45. G. Marcelin, C. Da Cunha, C. Gamblin, N. Suffee, C. Rouault, A. Leclerc, A. Lacombe, N. Sokolovska, E. L. Gautier, K. Clement, I. Dugail, Autophagy inhibition blunts PDGFRA adipose progenitors' cell-autonomous fibrogenic response to high-fat diet. *Autophagy* **16**, 2156–2166 (2020).
46. K. Dasuri, L. Zhang, P. Ebenezer, S. O. Fernandez-Kim, A. J. Bruce-Keller, L. I. Szweda, J. N. Keller, Proteasome alterations during adipose differentiation and aging: Links to impaired adipocyte differentiation and development of oxidative stress. *Free Radic. Biol. Med.* **51**, 1727–1735 (2011).
47. M. T. Bengoechea-Alonso, J. Ericsson, The ubiquitin ligase Fbxw7 controls adipocyte differentiation by targeting C/EBPalpha for degradation. *Proc. Natl. Acad. Sci. U.S.A.* **107**, 11817–11822 (2010).
48. M. Watanabe, H. Takahashi, Y. Saeki, T. Ozaki, S. Itoh, M. Suzuki, W. Mizushima, K. Tanaka, S. Hatakeyama, The E3 ubiquitin ligase TRIM23 regulates adipocyte differentiation via stabilization of the adipogenic activator PPARγ. *eLife* **4**, e05615 (2015).
49. H. Arimochi, Y. Sasaki, A. Kitamura, K. Yasutomo, Differentiation of preadipocytes and mature adipocytes requires PSMB8. *Sci. Rep.* **6**, 26791 (2016).
50. J. M. Lee, S. S. Choi, Y. H. Lee, K. W. Khim, S. Yoon, B.-G. Kim, D. Nam, P.-G. Suh, K. Myung, J. H. Choi, The E3 ubiquitin ligase TRIM25 regulates adipocyte differentiation via proteasome-mediated degradation of PPARγ. *Exp. Mol. Med.* **50**, 1–11 (2018).
51. H. Dou, Y. Duan, X. Zhang, Q. Yu, Q. Di, Y. Song, P. Li, Y. Gong, Aryl hydrocarbon receptor (AhR) regulates adipocyte differentiation by assembling CRL4B ubiquitin ligase to target PPARγ for proteasomal degradation. *J. Biol. Chem.* **294**, 18504–18515 (2019).
52. C. S. Hudak, H. S. Sul, Pref-1, a gatekeeper of adipogenesis. *Front. Endocrinol. (Lausanne)* **4**, 79 (2013).
53. C. E. Lowe, S. O'Rahilly, J. J. Rochford, Adipogenesis at a glance. *J. Cell Sci.* **124**, 2681–2686 (2011).
54. A. C. Massey, A. Follenzi, R. Kiffin, C. Zhang, A. M. Cuervo, Early cellular changes after blockage of chaperone-mediated autophagy. *Autophagy* **4**, 442–456 (2008).
55. S. Bolte, F. P. Cordelières, A guided tour into subcellular colocalization analysis in light microscopy. *J. Microsc.* **224**, 213–232 (2006).
56. P. Kirchner, M. Bourdenx, J. Madrigal-Matute, S. Tiano, A. Diaz, B. A. Bartholdy, B. Will, A. M. Cuervo, Proteome-wide analysis of chaperone-mediated autophagy targeting motifs. *PLOS Biol.* **17**, e3000301 (2019).

Acknowledgments: We thank L. Cervera Caries for assistance with R and Parvati B. for assistance with morphometry. We thank the Histology and Comparative Pathology, the Flow Cytometry (both P30CA013330, Einstein Cancer Center), and the Stable Isotope and Metabolomics (DK020541, Einstein-Mt. Sinai Diabetes Research Center) core facilities at Einstein. **Funding:** This work was supported by the National Institutes of Health [AG021904 (A.M.C.), AG054108 (A.M.C.), DK098408 (A.M.C.), AG031782 (A.M.C., R.S., and E.G.), T32GM007491 (Y.R.J.), and T32 AG023475 (M.M.)], the JPB Foundation (A.M.C.), the Glenn Foundation (A.M.C.), the Grace Science Foundation (S.K.), and Ministerio de Ciencia e Innovacion – Margarita Salas fellowship (A.M.-G.). **Author contributions:** Conceptualization: S.K. and A.M.C. Investigation: S.K., Y.R.J., K.L., S.D., A.M.-G., O.S.-F., and R.S. Resources: M.M. and E.G. Supervision: A.M.C. Writing—original draft: S.K. Writing—review and editing: S.K. and A.M.C. **Competing interests:** A.M.C. and E.G. are cofounders and scientific advisory board members of Selphagy Therapeutics (Life Biosciences). A.M.C. consults for Generian Pharmaceuticals and Cognition Therapeutics. These entities did not provide financial support for this study and had no role in study design, data collection and analysis, decision to publish, or preparation of the manuscript. All other authors declare that they have no competing interests. **Data and materials availability:** There are no restrictions on data availability in the manuscript. All the information is included in the manuscript. All main and supplementary figures have associated source data that are provided as an Excel worksheet organized by figures, and they include statistics along with exact *P* values. Transcriptomics data were deposited in GEO with accession GSE188494. This manuscript does not report original code. The LAMP2A $^{f/f}$ mice can be provided by A.M.C. pending scientific review and a completed material transfer agreement. The tools to study CMA (namely, CMA reporter and small-molecule CMA modulator) can be provided by A.M.C. pending scientific review and a completed material transfer agreement. Requests for the mice and CMA tools should be submitted to A.M.C.

Submitted 29 March 2022
Accepted 28 September 2022
Published 16 November 2022
10.1126/sciadv.abq2733